

A search for point sources of EeV photons

The Pierre Auger Collaboration⁹⁸

A. Aab⁴², P. Abreu⁶⁵, M. Aglietta⁵⁴, M. Ahlers⁹⁵, E.J. Ahn⁸³, I. Al Samarai²⁹,
I.F.M. Albuquerque¹⁷, I. Allekotte¹, J. Allen⁸⁷, P. Allison⁸⁹, A. Almela^{11, 8}, J. Alvarez Castillo⁵⁸,
J. Alvarez-Muñiz⁷⁶, R. Alves Batista⁴¹, M. Ambrosio⁴⁵, A. Aminaei⁵⁹, L. Anchordoqui^{96, 0},
S. Andringa⁶⁵, C. Aramo⁴⁵, F. Arqueros⁷³, H. Asorey¹, P. Assis⁶⁵, J. Aublin³¹, M. Ave⁷⁶,
M. Avenier³², G. Avila¹⁰, A.M. Badescu⁶⁹, K.B. Barber¹², J. Bäuml³⁸, C. Baus³⁸, J.J. Beatty⁸⁹,
K.H. Becker³⁵, J.A. Bellido¹², C. Berat³², X. Bertou¹, P.L. Biermann³⁹, P. Billoir³¹, F. Blanco⁷³,
M. Blanco³¹, C. Bleve³⁵, H. Blümer^{38, 36}, M. Boháčová²⁷, D. Boncioli⁵³, C. Bonifazi²³,
R. Bonino⁵⁴, N. Borodai⁶³, J. Brack⁸¹, I. Brancus⁶⁶, P. Brogueira⁶⁵, W.C. Brown⁸²,
P. Buchholz⁴², A. Bueno⁷⁵, M. Buscemi⁴⁵, K.S. Caballero-Mora^{56, 76, 90}, B. Caccianiga⁴⁴,
L. Caccianiga³¹, M. Candusso⁴⁶, L. Caramete³⁹, R. Caruso⁴⁷, A. Castellina⁵⁴, G. Cataldi⁴⁹,
L. Cazon⁶⁵, R. Cester⁴⁸, A.G. Chavez⁵⁷, S.H. Cheng⁹⁰, A. Chiavassa⁵⁴, J.A. Chinellato¹⁸,
J. Chudoba²⁷, M. Cilmo⁴⁵, R.W. Clay¹², G. Cocciolo⁴⁹, R. Colalillo⁴⁵, L. Collica⁴⁴,
M.R. Coluccia⁴⁹, R. Conceição⁶⁵, F. Contreras⁹, M.J. Cooper¹², S. Coutu⁹⁰, C.E. Covault⁷⁹,
A. Criss⁹⁰, J. Cronin⁹¹, A. Curutiu³⁹, R. Dallier^{34, 33}, B. Daniel¹⁸, S. Dasso^{5, 3}, K. Daumiller³⁶,
B.R. Dawson¹², R.M. de Almeida²⁴, M. De Domenico⁴⁷, S.J. de Jong^{59, 61}, J.R.T. de Mello
Neto²³, I. De Mitri⁴⁹, J. de Oliveira²⁴, V. de Souza¹⁶, L. del Peral⁷⁴, O. Deligny²⁹,
H. Dembinski³⁶, N. Dhital⁸⁶, C. Di Giulio⁴⁶, A. Di Matteo⁵⁰, J.C. Diaz⁸⁶, M.L. Díaz Castro¹⁸,
P.N. Diep⁹⁷, F. Diogo⁶⁵, C. Dobrigkeit¹⁸, W. Docters⁶⁰, J.C. D'Olivo⁵⁸, P.N. Dong^{97, 29},
A. Dorofeev⁸¹, Q. Dorosti Hasankiadeh³⁶, M.T. Dova⁴, J. Ebr²⁷, R. Engel³⁶, M. Erdmann⁴⁰,
M. Erfani⁴², C.O. Escobar^{83, 18}, J. Espadanal⁶⁵, A. Etchegoyen^{8, 11}, P. Facal San Luis⁹¹,
H. Falcke^{59, 62, 61}, K. Fang⁹¹, G. Farrar⁸⁷, A.C. Fauth¹⁸, N. Fazzini⁸³, A.P. Ferguson⁷⁹,
M. Fernandes²³, B. Fick⁸⁶, J.M. Figueira⁸, A. Filevich⁸, A. Filipčič^{70, 71}, B.D. Fox⁹², O. Fratu⁶⁹,
U. Fröhlich⁴², B. Fuchs³⁸, T. Fuji⁹¹, R. Gaior³¹, B. García⁷, S.T. Garcia Roca⁷⁶,
D. Garcia-Gamez³⁰, D. Garcia-Pinto⁷³, G. Garilli⁴⁷, A. Gascon Bravo⁷⁵, F. Gate³⁴,
H. Gemmeke³⁷, P.L. Ghia³¹, U. Giaccari²³, M. Giammarchi⁴⁴, M. Giller⁶⁴, C. Glaser⁴⁰,
H. Glass⁸³, F. Gomez Albarracin⁴, M. Gómez Berisso¹, P.F. Gómez Vitale¹⁰, P. Gonçalves⁶⁵,
J.G. Gonzalez³⁸, B. Gookin⁸¹, A. Gorgi⁵⁴, P. Gorham⁹², P. Gouffon¹⁷, S. Grebe^{59, 61},
N. Griffith⁸⁹, A.F. Grillo⁵³, T.D. Grubb¹², Y. Guardincerri³, F. Guarino⁴⁵, G.P. Guedes¹⁹,
P. Hansen⁴, D. Harari¹, T.A. Harrison¹², J.L. Harton⁸¹, A. Haungs³⁶, T. Hebbeker⁴⁰, D. Heck³⁶,
P. Heimann⁴², A.E. Herve³⁶, G.C. Hill¹², C. Hojvat⁸³, N. Hollon⁹¹, E. Holt³⁶, P. Homola^{42, 63},
J.R. Hörandel^{59, 61}, P. Horvath²⁸, M. Hrabovský^{28, 27}, D. Huber³⁸, T. Huege³⁶, A. Insolia⁴⁷,
P.G. Isar⁶⁷, K. Islo⁹⁶, I. Jandt³⁵, S. Jansen^{59, 61}, C. Jarne⁴, M. Josebachuili⁸, A. Kääpä³⁵,
O. Kambeitz³⁸, K.H. Kampert³⁵, P. Kasper⁸³, I. Katkov³⁸, B. Kégl³⁰, B. Keilhauer³⁶,

⁹⁸www.auger.org.ar; www.auger.org

⁹⁸Pierre Auger Collaboration, Av. San Martín Norte 306, 5613 Malargüe, Mendoza, Argentina

A. Keivani⁸⁵, E. Kemp¹⁸, R.M. Kieckhafer⁸⁶, H.O. Klages³⁶, M. Kleifges³⁷, J. Kleinfeller⁹,
 R. Krause⁴⁰, N. Krohm³⁵, O. Krömer³⁷, D. Kruppke-Hansen³⁵, D. Kuempel^{40, 35, 42}, N. Kunka³⁷,
 G. La Rosa⁵², D. LaHurd⁷⁹, L. Latronico⁵⁴, R. Lauer⁹⁴, M. Lauscher⁴⁰, P. Lautridou³⁴, S. Le
 Coz³², M.S.A.B. Leão¹⁴, D. Lebrun³², P. Lebrun⁸³, M.A. Leigui de Oliveira²²,
 A. Letessier-Selvon³¹, I. Lhenry-Yvon²⁹, K. Link³⁸, R. López⁵⁵, A. Lopez Agüera⁷⁶, K. Louedec³²,
 J. Lozano Bahilo⁷⁵, L. Lu^{35, 77}, A. Lucero⁸, M. Ludwig³⁸, H. Lyberis²³, M.C. Maccarone⁵²,
 M. Malacari¹², S. Maldera⁵⁴, J. Maller³⁴, D. Mandat²⁷, P. Mantsch⁸³, A.G. Mariazzi⁴, V. Marin³⁴,
 I.C. Mariş⁷⁵, G. Marsella⁴⁹, D. Martello⁴⁹, L. Martin^{34, 33}, H. Martinez⁵⁶, O. Martínez Bravo⁵⁵,
 D. Martraire²⁹, J.J. Masías Meza³, H.J. Mathes³⁶, S. Mathys³⁵, A.J. Matthews⁹⁴, J. Matthews⁸⁵,
 G. Matthiae⁴⁶, D. Maurel³⁸, D. Maurizio¹³, E. Mayotte⁸⁰, P.O. Mazur⁸³, C. Medina⁸⁰,
 G. Medina-Tanco⁵⁸, M. Melissas³⁸, D. Melo⁸, E. Menichetti⁴⁸, A. Menshikov³⁷, S. Messina⁶⁰,
 R. Meyhandan⁹², S. Mićanović²⁵, M.I. Micheletti⁶, L. Middendorf⁴⁰, I.A. Minaya⁷³,
 L. Miramonti⁴⁴, B. Mitrica⁶⁶, L. Molina-Bueno⁷⁵, S. Mollerach¹, M. Monasor⁹¹, D. Monnier
 Ragainne³⁰, F. Montanet³², C. Morello⁵⁴, J.C. Moreno⁴, M. Mostafá⁹⁰, C.A. Moura²²,
 M.A. Muller^{18, 21}, G. Müller⁴⁰, M. Münchmeyer³¹, R. Mussa⁴⁸, G. Navarra⁵⁴ †, S. Navas⁷⁵,
 P. Necesal²⁷, L. Nellen⁵⁸, A. Nelles^{59, 61}, J. Neuser³⁵, M. Niechciol⁴², L. Niemietz³⁵,
 T. Niggemann⁴⁰, D. Nitz⁸⁶, D. Nosek²⁶, V. Novotny²⁶, L. Nožka²⁸, L. Ochilo⁴², A. Olinto⁹¹,
 M. Oliveira⁶⁵, M. Ortiz⁷³, N. Pacheco⁷⁴, D. Pakk Selmi-Dei¹⁸, M. Palatka²⁷, J. Pallotta²,
 N. Palmieri³⁸, P. Papenbreer³⁵, G. Parente⁷⁶, A. Parra⁷⁶, S. Pastor⁷², T. Paul^{96, 88}, M. Pech²⁷,
 J. Pękala⁶³, R. Pelayo⁵⁵, I.M. Pepe²⁰, L. Perrone⁴⁹, R. Pesce⁴³, E. Petermann⁹³, C. Peters⁴⁰,
 S. Petretera^{50, 51}, A. Petrolini⁴³, Y. Petrov⁸¹, R. Piegai³, T. Pierog³⁶, P. Pieroni³, M. Pimenta⁶⁵,
 V. Pirronello⁴⁷, M. Platino⁸, M. Plum⁴⁰, A. Porcelli³⁶, C. Porowski⁶³, P. Privitera⁹¹,
 M. Prouza²⁷, V. Purrello¹, E.J. Quel², S. Querschfeld³⁵, S. Quinn⁷⁹, J. Rautenberg³⁵, O. Ravel³⁴,
 D. Ravignani⁸, B. Revenu³⁴, J. Ridky²⁷, S. Riggi^{52, 76}, M. Risse⁴², P. Ristori², V. Rizi⁵⁰,
 J. Roberts⁸⁷, W. Rodrigues de Carvalho⁷⁶, I. Rodriguez Cabo⁷⁶, G. Rodriguez Fernandez^{46, 76},
 J. Rodriguez Rojo⁹, M.D. Rodríguez-Frías⁷⁴, G. Ros⁷⁴, J. Rosado⁷³, T. Rossler²⁸, M. Roth³⁶,
 E. Roulet¹, A.C. Rovero⁵, C. Rühle³⁷, S.J. Saffi¹², A. Saftoiu⁶⁶, F. Salamida²⁹, H. Salazar⁵⁵,
 F. Salesa Greus⁹⁰, G. Salina⁴⁶, F. Sánchez⁸, P. Sanchez-Lucas⁷⁵, C.E. Santo⁶⁵, E. Santos⁶⁵,
 E.M. Santos¹⁷, F. Sarazin⁸⁰, B. Sarkar³⁵, R. Sarmiento⁶⁵, R. Sato⁹, N. Scharf⁴⁰, V. Scherini⁴⁹,
 H. Schieler³⁶, P. Schiffer⁴¹, A. Schmidt³⁷, O. Scholten⁶⁰, H. Schoorlemmer^{92, 59, 61}, P. Schovánek²⁷,
 A. Schulz³⁶, J. Schulz⁵⁹, S.J. Sciutto⁴, A. Segreto⁵², M. Settimo³¹, A. Shadkam⁸⁵,
 R.C. Shellard¹³, I. Sidelnik¹, G. Sigl⁴¹, O. Sima⁶⁸, A. Śmiałkowski⁶⁴, R. Šmída³⁶, G.R. Snow⁹³,
 P. Sommers⁹⁰, J. Sorokin¹², R. Squartini⁹, Y.N. Srivastava⁸⁸, S. Stanič⁷¹, J. Stapleton⁸⁹,
 J. Stasielak⁶³, M. Stephan⁴⁰, A. Stutz³², F. Suarez⁸, T. Suomijärvi²⁹, A.D. Supanitsky⁵,
 M.S. Sutherland⁸⁵, J. Swain⁸⁸, Z. Szadkowski⁶⁴, M. Szuba³⁶, O.A. Taborda¹, A. Tapia⁸,
 M. Tartare³², N.T. Thao⁹⁷, V.M. Theodoro¹⁸, J. Tiffenberg³, C. Timmermans^{61, 59}, C.J. Todero
 Peixoto¹⁵, G. Toma⁶⁶, L. Tomankova³⁶, B. Tomé⁶⁵, A. Tonachini⁴⁸, G. Torralba Elipe⁷⁶,
 D. Torres Machado³⁴, P. Travnicek²⁷, E. Trovato⁴⁷, M. Tüeros⁷⁶, R. Ulrich³⁶, M. Unger³⁶,
 M. Urban⁴⁰, J.F. Valdés Galicia⁵⁸, I. Valiño⁷⁶, L. Valore⁴⁵, G. van Aar⁵⁹, A.M. van den Berg⁶⁰,
 S. van Velzen⁵⁹, A. van Vliet⁴¹, E. Varela⁵⁵, B. Vargas Cárdenas⁵⁸, G. Varner⁹², J.R. Vázquez⁷³,

R.A. Vázquez⁷⁶, D. Veberič³⁰, V. Verzi⁴⁶, J. Vicha²⁷, M. Videla⁸, L. Villaseñor⁵⁷, B. Vlcek⁹⁶,
 S. Vorobiov⁷¹, H. Wahlberg⁴, O. Wainberg^{8, 11}, D. Walz⁴⁰, A.A. Watson⁷⁷, M. Weber³⁷,
 K. Weidenhaupt⁴⁰, A. Weindl³⁶, F. Werner³⁸, B.J. Whelan⁹⁰, A. Widom⁸⁸, L. Wiencke⁸⁰,
 B. Wilczyńska⁶³ †, H. Wilczyński⁶³, M. Will³⁶, C. Williams⁹¹, T. Winchen⁴⁰, D. Wittkowski³⁵,
 B. Wundheiler⁸, S. Wykes⁵⁹, T. Yamamoto⁹¹ *a*, T. Yapici⁸⁶, P. Younk⁸⁴, G. Yuan⁸⁵,
 A. Yushkov⁴², B. Zamorano⁷⁵, E. Zas⁷⁶, D. Zavrtnik^{71, 70}, M. Zavrtnik^{70, 71}, I. Zaw⁸⁷ *c*,
 A. Zepeda⁵⁶ *b*, J. Zhou⁹¹, Y. Zhu³⁷, M. Zimbres Silva¹⁸, M. Ziolkowski⁴²

⁰ Department of Physics and Astronomy, Lehman College, City University of New York, New York, USA

¹ Centro Atómico Bariloche and Instituto Balseiro (CNEA-UNCuyo-CONICET), San Carlos de Bariloche, Argentina

² Centro de Investigaciones en Láseres y Aplicaciones, CITEDEF and CONICET, Argentina

³ Departamento de Física, FCEyN, Universidad de Buenos Aires y CONICET, Argentina

⁴ IFLP, Universidad Nacional de La Plata and CONICET, La Plata, Argentina

⁵ Instituto de Astronomía y Física del Espacio (CONICET-UBA), Buenos Aires, Argentina

⁶ Instituto de Física de Rosario (IFIR) - CONICET/U.N.R. and Facultad de Ciencias Bioquímicas y Farmacéuticas U.N.R., Rosario, Argentina

⁷ Instituto de Tecnologías en Detección y Astropartículas (CNEA, CONICET, UNSAM), and National Technological University, Faculty Mendoza (CONICET/CNEA), Mendoza, Argentina

⁸ Instituto de Tecnologías en Detección y Astropartículas (CNEA, CONICET, UNSAM), Buenos Aires, Argentina

⁹ Observatorio Pierre Auger, Malargüe, Argentina

¹⁰ Observatorio Pierre Auger and Comisión Nacional de Energía Atómica, Malargüe, Argentina

¹¹ Universidad Tecnológica Nacional - Facultad Regional Buenos Aires, Buenos Aires, Argentina

¹² University of Adelaide, Adelaide, S.A., Australia

¹³ Centro Brasileiro de Pesquisas Físicas, Rio de Janeiro, RJ, Brazil

¹⁴ Faculdade Independente do Nordeste, Vitória da Conquista, Brazil

¹⁵ Universidade de São Paulo, Escola de Engenharia de Lorena, Lorena, SP, Brazil

¹⁶ Universidade de São Paulo, Instituto de Física, São Carlos, SP, Brazil

¹⁷ Universidade de São Paulo, Instituto de Física, São Paulo, SP, Brazil

¹⁸ Universidade Estadual de Campinas, IFGW, Campinas, SP, Brazil

¹⁹ Universidade Estadual de Feira de Santana, Brazil

²⁰ Universidade Federal da Bahia, Salvador, BA, Brazil

²¹ Universidade Federal de Pelotas, Pelotas, RS, Brazil

²² Universidade Federal do ABC, Santo André, SP, Brazil

²³ Universidade Federal do Rio de Janeiro, Instituto de Física, Rio de Janeiro, RJ, Brazil

²⁴ Universidade Federal Fluminense, EEIMVR, Volta Redonda, RJ, Brazil

²⁵ Rudjer Bošković Institute, 10000 Zagreb, Croatia

²⁶ Charles University, Faculty of Mathematics and Physics, Institute of Particle and Nuclear

- Physics, Prague, Czech Republic
- ²⁷ Institute of Physics of the Academy of Sciences of the Czech Republic, Prague, Czech Republic
- ²⁸ Palacky University, RCPTM, Olomouc, Czech Republic
- ²⁹ Institut de Physique Nucléaire d'Orsay (IPNO), Université Paris 11, CNRS-IN2P3, Orsay, France
- ³⁰ Laboratoire de l'Accélérateur Linéaire (LAL), Université Paris 11, CNRS-IN2P3, France
- ³¹ Laboratoire de Physique Nucléaire et de Hautes Energies (LPNHE), Universités Paris 6 et Paris 7, CNRS-IN2P3, Paris, France
- ³² Laboratoire de Physique Subatomique et de Cosmologie (LPSC), Université Grenoble-Alpes, CNRS/IN2P3, France
- ³³ Station de Radioastronomie de Nançay, Observatoire de Paris, CNRS/INSU, France
- ³⁴ SUBATECH, École des Mines de Nantes, CNRS-IN2P3, Université de Nantes, France
- ³⁵ Bergische Universität Wuppertal, Wuppertal, Germany
- ³⁶ Karlsruhe Institute of Technology - Campus North - Institut für Kernphysik, Karlsruhe, Germany
- ³⁷ Karlsruhe Institute of Technology - Campus North - Institut für Prozessdatenverarbeitung und Elektronik, Karlsruhe, Germany
- ³⁸ Karlsruhe Institute of Technology - Campus South - Institut für Experimentelle Kernphysik (IEKP), Karlsruhe, Germany
- ³⁹ Max-Planck-Institut für Radioastronomie, Bonn, Germany
- ⁴⁰ RWTH Aachen University, III. Physikalisches Institut A, Aachen, Germany
- ⁴¹ Universität Hamburg, Hamburg, Germany
- ⁴² Universität Siegen, Siegen, Germany
- ⁴³ Dipartimento di Fisica dell'Università and INFN, Genova, Italy
- ⁴⁴ Università di Milano and Sezione INFN, Milan, Italy
- ⁴⁵ Università di Napoli "Federico II" and Sezione INFN, Napoli, Italy
- ⁴⁶ Università di Roma II "Tor Vergata" and Sezione INFN, Roma, Italy
- ⁴⁷ Università di Catania and Sezione INFN, Catania, Italy
- ⁴⁸ Università di Torino and Sezione INFN, Torino, Italy
- ⁴⁹ Dipartimento di Matematica e Fisica "E. De Giorgi" dell'Università del Salento and Sezione INFN, Lecce, Italy
- ⁵⁰ Dipartimento di Scienze Fisiche e Chimiche dell'Università dell'Aquila and INFN, Italy
- ⁵¹ Gran Sasso Science Institute (INFN), L'Aquila, Italy
- ⁵² Istituto di Astrofisica Spaziale e Fisica Cosmica di Palermo (INAF), Palermo, Italy
- ⁵³ INFN, Laboratori Nazionali del Gran Sasso, Assergi (L'Aquila), Italy
- ⁵⁴ Osservatorio Astrofisico di Torino (INAF), Università di Torino and Sezione INFN, Torino, Italy
- ⁵⁵ Benemérita Universidad Autónoma de Puebla, Puebla, Mexico
- ⁵⁶ Centro de Investigación y de Estudios Avanzados del IPN (CINVESTAV), México, Mexico
- ⁵⁷ Universidad Michoacana de San Nicolas de Hidalgo, Morelia, Michoacan, Mexico

- ⁵⁸ Universidad Nacional Autonoma de Mexico, Mexico, D.F., Mexico
- ⁵⁹ IMAPP, Radboud University Nijmegen, Netherlands
- ⁶⁰ KVI - Center for Advanced Radiation Technology, University of Groningen, Netherlands
- ⁶¹ Nikhef, Science Park, Amsterdam, Netherlands
- ⁶² ASTRON, Dwingeloo, Netherlands
- ⁶³ Institute of Nuclear Physics PAN, Krakow, Poland
- ⁶⁴ University of Łódź, Łódź, Poland
- ⁶⁵ Laboratório de Instrumentação e Física Experimental de Partículas - LIP and Instituto Superior Técnico - IST, Universidade de Lisboa - UL, Portugal
- ⁶⁶ 'Horia Hulubei' National Institute for Physics and Nuclear Engineering, Bucharest- Magurele, Romania
- ⁶⁷ Institute of Space Sciences, Bucharest, Romania
- ⁶⁸ University of Bucharest, Physics Department, Romania
- ⁶⁹ University Politehnica of Bucharest, Romania
- ⁷⁰ Experimental Particle Physics Department, J. Stefan Institute, Ljubljana, Slovenia
- ⁷¹ Laboratory for Astroparticle Physics, University of Nova Gorica, Slovenia
- ⁷² Institut de Física Corpuscular, CSIC-Universitat de València, Valencia, Spain
- ⁷³ Universidad Complutense de Madrid, Madrid, Spain
- ⁷⁴ Universidad de Alcalá, Alcalá de Henares (Madrid), Spain
- ⁷⁵ Universidad de Granada and C.A.F.P.E., Granada, Spain
- ⁷⁶ Universidad de Santiago de Compostela, Spain
- ⁷⁷ School of Physics and Astronomy, University of Leeds, United Kingdom
- ⁷⁹ Case Western Reserve University, Cleveland, OH, USA
- ⁸⁰ Colorado School of Mines, Golden, CO, USA
- ⁸¹ Colorado State University, Fort Collins, CO, USA
- ⁸² Colorado State University, Pueblo, CO, USA
- ⁸³ Fermilab, Batavia, IL, USA
- ⁸⁴ Los Alamos National Laboratory, Los Alamos, NM, USA
- ⁸⁵ Louisiana State University, Baton Rouge, LA, USA
- ⁸⁶ Michigan Technological University, Houghton, MI, USA
- ⁸⁷ New York University, New York, NY, USA
- ⁸⁸ Northeastern University, Boston, MA, USA
- ⁸⁹ Ohio State University, Columbus, OH, USA
- ⁹⁰ Pennsylvania State University, University Park, PA, USA
- ⁹¹ University of Chicago, Enrico Fermi Institute, Chicago, IL, USA
- ⁹² University of Hawaii, Honolulu, HI, USA
- ⁹³ University of Nebraska, Lincoln, NE, USA
- ⁹⁴ University of New Mexico, Albuquerque, NM, USA
- ⁹⁵ University of Wisconsin, Madison, WI, USA
- ⁹⁶ University of Wisconsin, Milwaukee, WI, USA

⁹⁷ Institute for Nuclear Science and Technology (INST), Hanoi, Vietnam

(‡) Deceased

(a) Now at Konan University

(b) Also at the Universidad Autonoma de Chiapas on leave of absence from Cinvestav

(c) Now at NYU Abu Dhabi

ABSTRACT

Measurements of air showers made using the hybrid technique developed with the fluorescence and surface detectors of the Pierre Auger Observatory allow a sensitive search for point sources of EeV photons anywhere in the exposed sky. A multivariate analysis reduces the background of hadronic cosmic rays. The search is sensitive to a declination band from -85° to $+20^\circ$, in an energy range from $10^{17.3}$ eV to $10^{18.5}$ eV. No photon point source has been detected. An upper limit on the photon flux has been derived for every direction. The mean value of the energy flux limit that results from this, assuming a photon spectral index of -2 , is $0.06 \text{ eV cm}^{-2} \text{ s}^{-1}$, and no celestial direction exceeds $0.25 \text{ eV cm}^{-2} \text{ s}^{-1}$. These upper limits constrain scenarios in which EeV cosmic ray protons are emitted by non-transient sources in the Galaxy.

Subject headings: astroparticle physics; cosmic rays; methods: data analysis

1. Introduction

A direct way to identify the origins of cosmic rays is to find fluxes of photons (gamma rays) coming from discrete sources. This method has been used to identify several likely sources of cosmic rays up to about 100 TeV in the Galaxy (Fermi-LAT Collaboration 2013). At sufficiently high energies, such photons must be produced primarily by π^0 decays, implying the existence of high-energy hadrons that cause the production of π^0 mesons at or near the source. It is not known whether the Galaxy produces cosmic rays at EeV energies ($1 \text{ EeV} = 10^{18} \text{ eV}$). An argument in favor is that the “ankle” of the cosmic-ray energy spectrum near 5 EeV is the only concave upward feature, and the transition from a Galactic power-law behavior to an extragalactic contribution should be recognizable as just such a spectral hardening (Hillas 1984). The ankle can be explained alternatively as a “dip” due to e^\pm pair production in a cosmic-ray spectrum that is dominated by protons of extragalactic origin. In that case, detectable sources of EeV protons would not be expected in the Galaxy (Berezinsky *et al.* 2006).

Protons are known to constitute at least a significant fraction of the cosmic rays near the ankle of the energy spectrum (The Pierre Auger Collaboration 2012a, 2010a, 2013). Those protons are able to produce photons with energies near 1 EeV by pion photoproduction or inelastic nuclear collisions near their sources. A source within the Galaxy could then be identified by a flux of photons arriving from a single direction.

The search here is for fluxes of photons with energies from $10^{17.3}$ eV up to $10^{18.5}$ eV. The energy range is chosen to account for high event statistics and to avoid additional shower development processes that may introduce a bias at highest energies (Homola & Risse 2007).

The Pierre Auger Observatory (The Pierre Auger Collaboration 2004) has excellent sensitivity to EeV photon fluxes due to its vast collecting area and its ability to discriminate between photons and hadronic cosmic rays (The Pierre Auger Collaboration 2009). The surface detector array (SD) (The Pierre Auger Collaboration 2008a) consists of 1660 water-Cherenkov detectors spanning 3000 km^2 on a regular grid of triangular cells with 1500 m spacing between nearest neighbor stations. It is located at latitude -35.2° in Mendoza Province, Argentina. Besides the surface array, there are 27 telescopes of the air fluorescence detector (FD) (The Pierre Auger Collaboration 2010b) located at five sites on the perimeter of the array. The FD is used to measure the longitudinal development of air showers above the surface array. The signals in the water-Cherenkov detectors are used to obtain the secondary particle density at ground measured as a function of distance to the shower core. The analysis presented in this work uses showers measured in hybrid mode (detected by at least one FD telescope and one SD station). The hybrid measurement technique provides a precise geometry and energy determination with a lower energy detection threshold compared to SD only measurements (The Pierre Auger Collaboration 2010b). Moreover, multiple characteristics of photon-induced air showers can be exploited by the two detector systems in combination, e.g., muon-poor ground signal and large depth of shower maximum compared to hadronic cosmic rays of the same energy. Several photon-hadron discriminating observables are defined and combined in a multivariate analysis (MVA) to search for photon point sources and to place directional upper limits on the photon flux over the celestial sphere up to declination $+20^\circ$.

The sensitivity depends on the declination of a target direction. For the median exposure, a flux of $0.14 \text{ photons km}^{-2} \text{ yr}^{-1}$ or greater would yield an excess of at least 5σ . This corresponds to an energy flux of $0.25 \text{ eV cm}^{-2} \text{ s}^{-1}$ for a photon flux following a $1/E^2$ spectrum, similar to energy fluxes of sources measured by TeV gamma-ray detectors. This is relevant because the energy flux per decade is the same in each energy decade for a source with a $1/E^2$ spectrum, and Fermi acceleration leads naturally to such a type of spectrum (cf. Sec. 8). The Auger Observatory has the sensitivity to detect photon fluxes from such

hypothetical EeV cosmic-ray sources in the Galaxy.

At EeV energies, fluxes of photons are attenuated over intergalactic distances by e^\pm pair production in collisions of those photons with cosmic-background photons. The e^\pm can again interact with background photons via inverse-Compton scattering, resulting in an electromagnetic cascade that ends at GeV-TeV energies. The detectable volume of EeV photon sources is small compared to the Greisen-Zatsepin-Kuz'min (GZK) sphere (Greisen 1966; Zatsepin & Kuz'min 1966), but large enough to encompass the Milky Way, the Local Group of galaxies and possibly Centaurus A, given an attenuation length of about 4.5 Mpc at EeV energies (Homola & Risse 2007; De Angelis *et al.* 2013; Settimo & De Domenico 2013).

The present study targets all exposed celestial directions without prejudice. It is a “blind” search to see if there might be an indication of a photon flux from any direction. One or more directions of significance might be identified for special follow-up study with future data. Because there is a multitude of “trials,” some excesses are likely to occur by chance. A genuine modest flux would not be detectable in this kind of blind search. The possible production of ultra-high energy photons and neutrons has been studied extensively in relation to some directions in the Galaxy (Medina Tanco & Watson 2001; Bossa *et al.* 2003; Aharonian & Neronov 2005; Crocker *et al.* 2005; Gupta *et al.* 2012).

The Auger Collaboration has published stringent upper limits on the *diffuse* intensity of photons at ultra-high energies (The Pierre Auger Collaboration 2007, 2008b, 2009; Settimo 2011). Those limits impose severe constraints on “top-down” models for the production of ultra-high energy cosmic rays. At the energies in this study, however, the limits do not preclude photon fluxes of a strength that would be detectable from discrete directions.

The paper is organized as follows: in Sec. 2, mass composition-sensitive observables are introduced, exploiting information from the surface detector as well as from the fluorescence telescopes. These observables are combined in a multivariate analysis explained in Sec. 3, before introducing the dataset and applied quality cuts in Sec. 4. A calculation of the expected isotropic background contribution is described in Sec. 5. A blind search technique and an upper limit calculation are explained in Sec. 6 and Sec. 7, respectively. Finally, results are shown and discussed in Sec. 8.

2. Mass composition-sensitive observables

The strategy in searching for directional photon point sources is based on the selection of a subset of photon-like events, to reduce the isotropic hadronic background. Such a selection relies on the combination of several mass composition-sensitive parameters, using

a multivariate analysis (MVA).

Once the MVA training is defined, the photon-like event selection is optimized direction-wise, accounting for the expected background contribution from a given target direction to take into account the contribution of different trigger efficiencies.

Profiting from the hybrid nature of the Auger Observatory, we make use of FD- and SD-based observables, which provide complementary information on the longitudinal and lateral distributions of particles in the showers, respectively. By means of Monte Carlo (MC) simulations, five observables are selected to optimize the signal (photon) selection efficiency against the background (hadron) rejection power. The selected observables are described below in detail.

2.1. FD observables

A commonly used mass-composition sensitive observable is the depth of the shower maximum X_{\max} , which is defined as the atmospheric depth at which the longitudinal development of a shower reaches its maximum in terms of energy deposit. Given their mostly electromagnetic nature, on average, photon-induced air showers develop deeper in the atmosphere, compared to hadron-induced ones of similar energies, resulting in larger X_{\max} values. The difference is about 100 g cm^{-2} in the energy range discussed in this paper. The reconstruction procedure is based on the fit of the Gaisser-Hillas function (Gaisser & Hillas 1977) to the energy deposit profile, which has been proven to provide a good description of the Extensive Air Shower (EAS) independently of the primary type.

In addition to the Gaisser-Hillas function, the possibility of fitting the longitudinal profile with the Greisen function (Greisen 1956) has been explored. The Greisen function was originally introduced to describe the longitudinal profile of pure electromagnetic showers: a better fit to the longitudinal profile is thus expected for photon-initiated showers when compared to nuclear ones of the same primary energy. The $\chi_{\text{Gr}}^2/\text{dof}$ is used to quantify the goodness of the fit and as potential discriminating observable. The Greisen function has one free parameter, that is the primary energy E_{Gr} , which is also influenced by the primary particle. The observable is $E_{\text{Gr}}/E_{\text{GH}}$, where E_{GH} is the energy obtained by integrating the Gaisser-Hillas function. All of the X_{\max} , the $\chi_{\text{Gr}}^2/\text{dof}$ and the $E_{\text{Gr}}/E_{\text{GH}}$ are used as variables contributing to the photon-hadron classifier. The method adopted for the classification, as well as the relative weight of each variable to the classification process, will be discussed in the next section.

2.2. SD observables

When observed at ground, photon-induced showers have a generally steeper lateral distribution than nuclear primaries because of the almost absent muon component. It is worth noting that, as a consequence of the trigger definition in the local stations and of the station spacing in the array (The Pierre Auger Collaboration 2010c), the surface detector alone is not fully efficient in the energy range used in this work. Thus, as opposed to previous work based on SD observables (The Pierre Auger Collaboration 2008b), we adopt here observables that are defined at the station level and which do not necessarily require an independent reconstruction in SD mode. Such observables are related to an estimator (S_b) of the lateral distribution of the signal or to the shape of the flash analog digital converter (FADC) trace in individual stations.

The S_b parameter is sensitive to different lateral distribution functions, due to the presence/absence of the flatter muon component (Ros *et al.* 2011), and has already been used in previous studies (Settimo 2011). It is defined as

$$S_b = \sum_{i=1}^N \left[S_i \cdot \left(\frac{r_i}{1000 \text{ m}} \right)^b \right], \quad (1)$$

where the sum extends over all N triggered stations, S_i expresses the signal strength of the i -th SD station, r_i the distance of this station to the shower axis, and b a variable exponent. It has been found that, in the energy region of interest, the optimized b for photon-hadron separation is $b = 3$ (Ros *et al.* 2013).

As a result of both the smaller signal in the stations, on average, and the steeper lateral distribution function, smaller values of S_b are expected for photon primaries. To prevent a possible underestimate of S_b (which would mimic the behavior of a photon-like event), due to missing stations during the deployment of the array or temporarily inefficient stations, events are selected requiring at least 4 active stations (fully operational, but not necessary triggered) within 2 km from the core.

Other observables, containing information on the fraction of electromagnetic and muonic components at the ground, are related to measurements of the time structure derived from the FADC traces in the SD. The spread of the arrival times of shower particles at a fixed distance from the shower axis increases for smaller production heights, i.e., closer to the detector station. Consequently, a larger spread is expected in case of deep developing primaries (i.e., photons). Here we introduce the shape parameter, defined as the ratio of the early-arriving to the late-arriving integrated signal as a function of time measured in the water-Cherenkov

detector with the strongest signal:

$$\text{ShapeP}(r, \theta) = \frac{S_{\text{early}}(r, \theta)}{S_{\text{late}}(r, \theta)}. \quad (2)$$

The early signal S_{early} is defined as the integrated signal over time bins less than a scaled time $t_i^{\text{scaled}} \leq 0.6 \mu\text{s}$, beginning from the signal start moment. The scaled time varies for different inclination angles θ and distances r to the shower axis and can be expressed as:

$$t_i^{\text{scaled}}(r, \theta) = t_i \cdot \frac{r_0}{r} \cdot \frac{1}{c_1 + c_2 \cdot \cos(\theta)}, \quad (3)$$

where t_i is the real time of bin i and $r_0 = 1000$ m is a reference distance. $c_1 = -0.6$ and $c_2 = 1.9$ are scaling parameters to average traces over different inclination angles. Correspondingly, the late signal S_{late} is the integrated signal over time bins later than $t_i^{\text{scaled}} > 0.6 \mu\text{s}$, until signal end.

3. Multivariate analysis

The selected discriminating observables are combined by a multivariate analysis technique to enhance and maximize their photon-hadron separation power. In particular, the analysis was developed by using a Boosted Decision Tree (BDT) as classifier (Breiman *et al.* 1984; Schapire 1990). Several other classifiers were also tested, but the BDT stands out due to the simplicity of the method, where each training step involves a one-dimensional cut optimization, in conjunction with high-performance photon-hadron discrimination (Kuempel 2011). Another advantage of BDTs is that they are insensitive to the inclusion of poorly discriminating variables. The observables were selected from a larger sample of SD and hybrid observables by looking at their individual discrimination power in different energy and zenith bins, their strength in the BDT, and the stability of the results. One benchmark quantity that assess the performance of BDTs is the separation. It is defined to be zero for identical signal and background shapes of the output response, and it is one for shapes with no overlap. The overall separation as well as the separation if excluding a specific observable from the analysis is listed in Table 1. The most significant variables contributing to the BDT are X_{max} and S_b . With these variables alone we achieve a separation of 0.654. During the classification process the BDT handles the correlation of the observables to energy and zenith angle of the primary particle by including them as additional parameters.

For the classification process, BDTs are trained and tested using MC simulations. Air showers are simulated using the CORSIKA v. 6.900 (Heck *et al.* 1998) code. A total number of $\sim 30,000$ photon and $\sim 60,000$ proton primaries are generated according

Table 1: Overall separation of the observables using BDTs (*all*) as well as the remaining separation if excluding a single observable from the MVA.

<i>Observables</i>	<i>Separation</i>
all	0.668
No S_b	0.438
No X_{\max}	0.599
No $\chi_{\text{Gr}}^2/\text{dof}$	0.662
No $E_{\text{Gr}}/E_{\text{GH}}$	0.664
No ShapeP	0.667

to a power-law spectrum of index -2.7 between $10^{17.2}$ eV and $10^{18.5}$ eV, using QGSJET-01c (Kalmykov & Ostapchenko 1989) and GHEISHA (Fesefeldt 1985) as high- and low-energy interaction models, respectively. The impact of different hadronic interaction models is discussed in Sec. 8. The detector response was simulated using the simulation chain developed within the offline framework (Argiro *et al.* 2007), as discussed in (Settimo 2012). The same reconstruction chain and the same selection criteria as for data (discussed in Sec. 4) were then applied. During the classification phase, photon and proton showers are reweighted according to a spectral index of -2.0 and -3.0, respectively. The impact of a changing photon spectral index on the results is discussed in Sec. 8. The distribution of observables for photon and proton simulations for a specific energy and zenith range is shown in Fig. 1. The MVA output response value is named β and shown in Fig. 2 for the training and testing samples. Note that the β distribution is by construction limited to the range $[-1, 1]$.

4. Dataset

The search for photon point sources is performed on the sample of hybrid events collected between January 2005 and September 2011, under stable data-taking conditions. Events are selected requiring a reconstructed energy between $10^{17.3}$ eV and $10^{18.5}$ eV, where the energy is determined as the calorimetric one plus a 1% missing energy correction associated with photon primaries (Barbosa *et al.* 2004). To ensure good energy and directional reconstruction, air showers with zenith angle smaller than 60° and with a good reconstruction of the shower geometry are selected. For a reliable profile reconstruction we require: a reduced χ^2 of the longitudinal profile fit to the Gaisser-Hillas function smaller than 2.5, a Cherenkov light contamination smaller than 50%, and an uncertainty of the reconstructed energy less than 40%. Overcast cloud conditions can distort the light profiles of EAS and influence

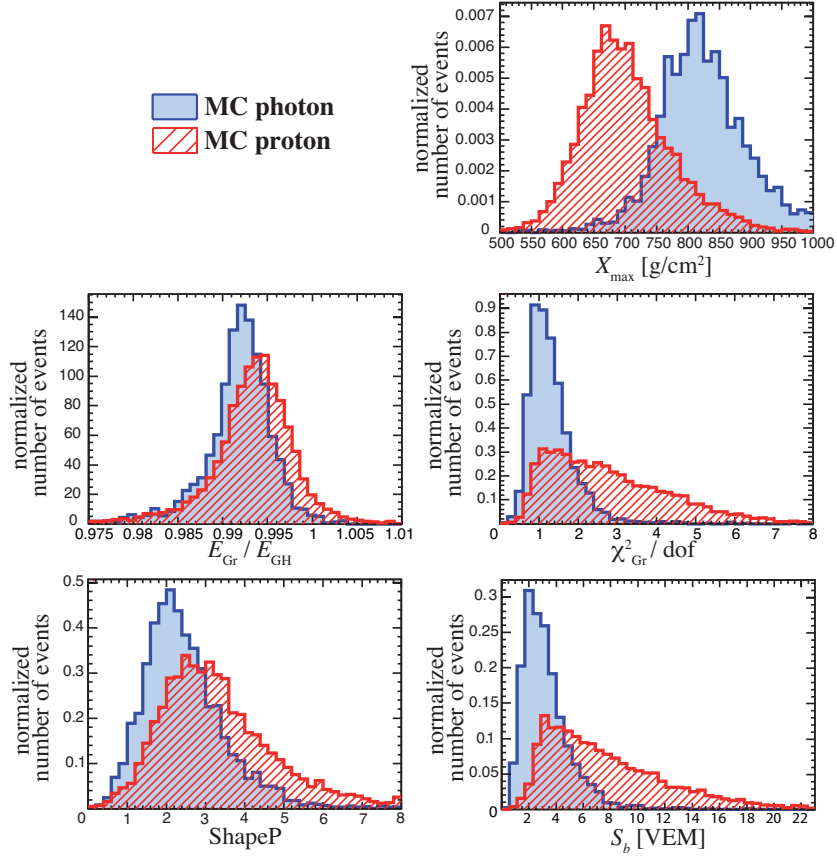


Fig. 1.— Distributions of photon (full blue) and proton (striated red) simulations of the introduced observables. The distributions are shown as examples for the energy range between $10^{17.6}$ eV and 10^{18} eV and zenith angle between 0° and 30° .

also the hybrid exposure calculation (Chirinos 2013). To reject misreconstructed profiles, we select only periods with a detected cloud coverage $\leq 80\%$ with a cut efficiency of 91%. In addition, only events with a reliable measurement of the vertical optical depth of aerosols are selected (BenZvi *et al.* 2007). As already mentioned, at least 4 active stations are required within 2 km of the hybrid-reconstructed axis to prevent an underestimation of S_b . To enrich our sample with deep showers, we do not require that X_{\max} has been observed within the field of view. This cut is usually applied to assure a good X_{\max} resolution (e.g. (The Pierre Auger Collaboration 2009, 2010d,a)), but for this analysis we focus on a maximization of the acceptance for photon showers. Profiles, for which only the rising edge is observed are certain to have a deep X_{\max} below ground level ($\sim 840/\cos(\theta)$ g/cm 2). Shallow showers, that are also enriched by the release of this cut, can be easily removed in later stages of the analysis by the MVA β cut (cf. Sec. 6). The photon X_{\max} resolution with this type

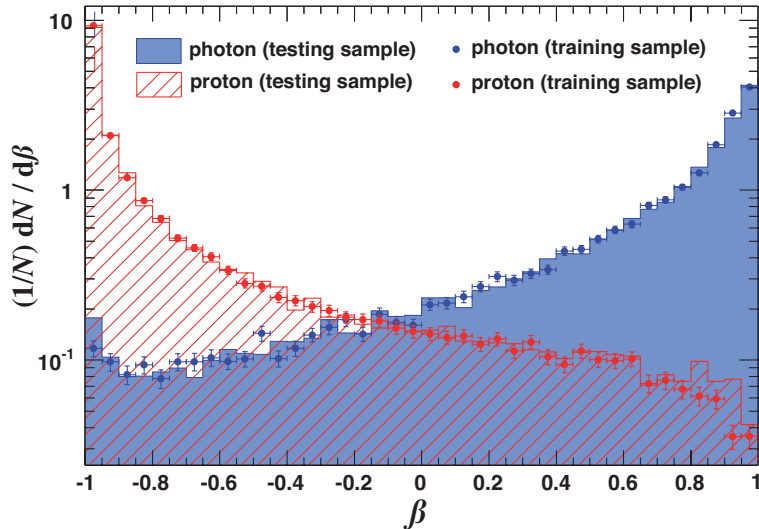


Fig. 2.— Multivariate analysis response value β for photon and proton primaries using boosted decision trees. During evaluation the MC sample is split half into a training (filled circles) and half into a testing sample (solid line).

of selection increases from 39 to 53 g/cm², but the photon acceptance is increased by 42%. The energy resolution is about 20%, independently of the primary mass. These resolutions do not affect significantly the analysis since the trace of photons from a point source is an accumulation of events from a specific direction, and the event direction is well reconstructed also with the relaxed cuts: as shown in Fig. 3, the angular resolution is about 0.7°. We also verified that the separation power of the MVA is not significantly modified by the weaker selection requirements.

After selection, the final dataset consists of $N_{\text{data}} = 241,466$ events with an average energy of $10^{17.7}$ eV. In fact, the energy distribution of these events expresses a compensation effect of the energy spectral index and trigger inefficiencies at low energies. A discussion of the hybrid trigger efficiency for hadrons in the energy range below 10^{18} eV is given in (Settimo 2012). In Sec. 7 this discussion is extended to the case of photons. The average number of triggered stations in the current dataset is 2 at $10^{17.5}$ eV, where the bulk of events is detected, generally increasing with zenith angle and with energy (up to 4 between 10^{18} eV and $10^{18.5}$ eV).

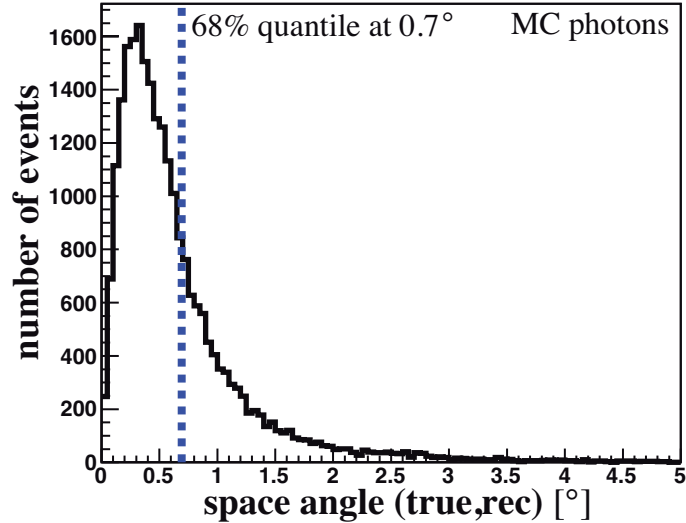


Fig. 3.— Space angle distribution between simulated and reconstructed arrival direction of photon primaries. The angular resolution is calculated as the 68% quantile located at 0.7° denoted by the dotted line.

5. Background expectation

The contribution of an isotropic background is estimated using the scrambling technique (Cassiday *et al.* 1990). This method has the advantage of using only measured data and takes naturally into account detector efficiencies and aperture features. Therefore, it is not sensitive to the (unknown) cosmic ray mass composition in the covered energy range.

As a first step, the arrival directions (in local coordinates) of the events are smeared randomly according to their individual reconstruction uncertainty. In a second step, N_{data} events are formed by choosing randomly a local coordinate and, independently, a Coordinated Universal Time from the pool of measured directions and times. This procedure is repeated 5,000 times. The mean number of arrival directions within a target is then used as the expected number for that particular sky location. As each telescope has a different azimuthal trigger probability, events are binned by telescope before scrambling. The number of events observed in each telescope varies between 4,358 and 14,100. Since the scrambling technique is less effective in the southern celestial pole region¹, declinations $< -85^\circ$ are omitted from the analysis.

¹At the pole, the estimated background would always be similar to the observed signal. Therefore a possible excess or deficit of cosmic rays from the pole would always be masked.

Sky maps are pixelized using the HEALPix software (Gorski *et al.* 2005). Target centers are taken as the central points of a HEALPix grid using $N_{\text{side}} = 256$ (target separation $\sim 0.3^\circ$), resulting in 526,200 target centers south of a declination of $+20^\circ$. The treatment of arrival directions is based on an unbinned analysis, i.e., angular distances are calculated analytically. For each target direction, we use a top-hat counting region of 1° (selecting events within a hard cut on angle from the target center), motivated to account for low event statistics (cf. (Alexandreas *et al.* 1993)) and a possible non-Gaussian tail of the error distribution².

The expected directional background contribution for the covered search period is shown in Fig. 4. There is an azimuthal asymmetry in the expected background as a result of a seasonally-dependent duty cycle, i.e., during austral summer, data taking using the fluorescence telescopes is reduced compared to austral winter (Settimo 2012; The Pierre Auger Collaboration 2011a).

6. Blind search analysis

When performing the blind search analysis, we use only a subset of the recorded data, selected as “photon-like” according to the β distribution. The definition of “photon-like” (i.e., the β_{cut} position when selecting events with $\beta \geq \beta_{\text{cut}}$) is related to the MC photon and the data efficiencies, ε_γ^β and $\varepsilon_{\text{data}}^\beta$, respectively, and to the expected number of background events $n_b(\alpha, \delta)$ which is a function of the celestial coordinates α and δ . The efficiencies ε_γ^β and $\varepsilon_{\text{data}}^\beta$ are shown in Fig. 5 as a function of the multivariate cut β_{cut} . To estimate $\varepsilon_{\text{data}}^\beta$ more accurately, a declination dependence is taken into account, $\varepsilon_{\text{data}}^\beta = \varepsilon_{\text{data}}^\beta(\delta)$, indicated by the red shaded area in Fig. 5. The expectation of a purely hadronic composition is shown as a grey band. To improve the detection potential of photons from point sources, the cut on the β distribution is optimized, dependent on the direction of a target center or, more specifically, dependent on the expected number of background events $n_b(\alpha, \delta)$. In this way the background contamination is reduced while keeping most of the signal events in the dataset. This optimization procedure can be described as follows: the upper limit of photons n_s from a point source at a given direction is calculated under the assumption that $n_{\text{data}} = n_b^\beta$, i.e., when the observed number of events (n_{data}) is equal to the expected number (cf. Sec. 5). The expected number of events after cutting on the β distribution can be estimated as $n_b^\beta(\alpha, \delta) = n_b(\alpha, \delta) \cdot \varepsilon_{\text{data}}^\beta(\delta)$ and is typically less than 4 events for the β_{cut} values

²It was verified that selecting containment radii of 0.74° and 1.5° increases the mean flux upper limit of point sources by +9% and +11%, respectively.

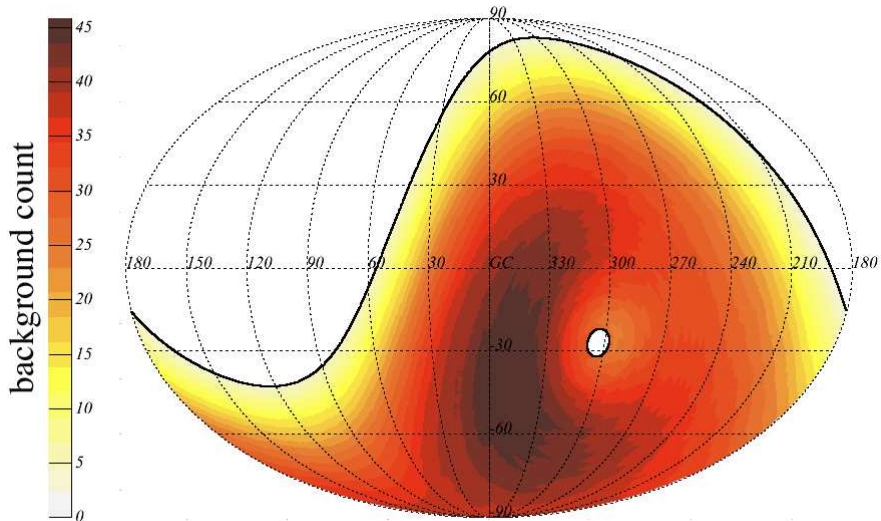


Fig. 4.— Sky map of the expected background contribution (average of 5,000 scrambled maps) in Galactic coordinates using the Mollweide-projection (Bugayevskiy & Snyder 1995). The solid black lines indicate the covered declination range between -85° and $+20^\circ$. Note that the southern celestial pole region is omitted in this analysis for reasons explained in Sec. 5.

finally chosen. There are several ways to define an upper limit on the number of photons n_s , at a given confidence level (CL) in the presence of a Poisson-distributed background. Here the procedure of Zech (Zech 1989) is utilized, where n_s is given by:

$$P(\leq n_b^\beta | n_b^\beta + n_s) = \alpha_{\text{CL}} \cdot P(\leq n_b^\beta | n_b^\beta), \quad (4)$$

with $\alpha_{\text{CL}} \equiv 1 - \text{CL} = 0.05$, and where the expected background contribution is n_b^β (cf. (The Pierre Auger Collaboration 2012b)). The frequentist interpretation of the above equation is as follows: “For an infinitely large number of repeated experiments looking for a signal with expectation n_s and background with mean n_b^β , where the background contribution is restricted to a value less than or equal to n_b^β , the frequency of observing n_b^β or fewer events is α_{CL} .” Since n_b^β is not an integer in general, a linear interpolation is applied to calculate the Poisson expectation. To determine the optimized β_{cut} , the sensitivity is maximized by minimizing the expected upper limit by scanning over the entire range of possible β_{cut} , also taking into account the photon efficiency ε_γ^β :

$$\min \left(\frac{n_s(\beta_{\text{cut}})}{\varepsilon_\gamma^\beta(\beta_{\text{cut}})} \right) \quad \text{with } \beta_{\text{cut}} \in [-1, 1]. \quad (5)$$

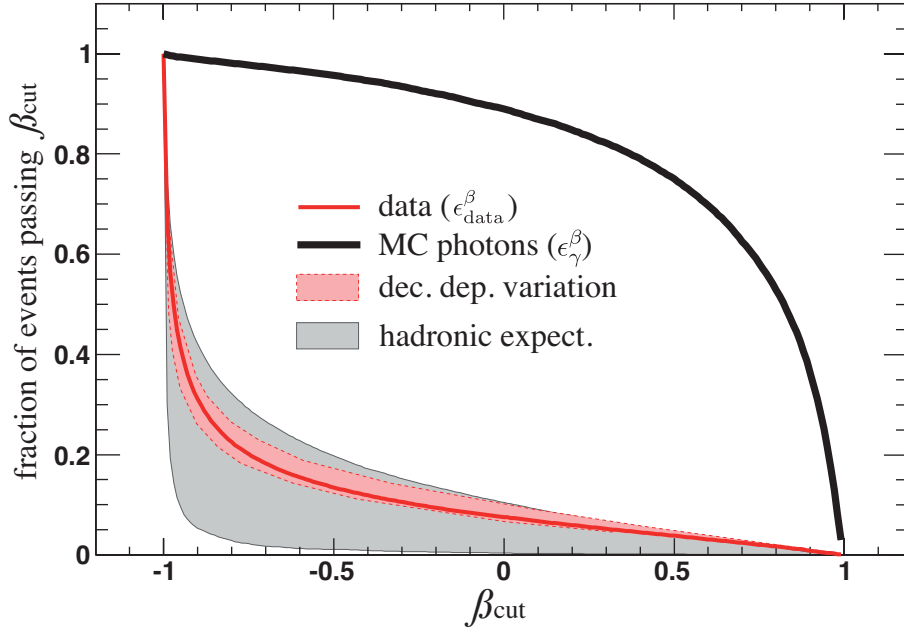


Fig. 5.— Fraction of events passing the β_{cut} for simulated primary photons (black) and measured averaged data (red). The red shaded area represents the declination-dependent variation of the data. The grey shaded area represents the expectation of a purely hadronic composition derived from MC simulations.

The optimized mean β_{cut} is shown in Fig. 6 as a function of the expected background contribution. The grey area indicates the declination-dependent variation of the optimization. The mean β_{cut} value used in this analysis is 0.22 resulting in an average background contribution after β_{cut} of 1.48 events. Applying the optimized β_{cut} to measured data reduces the dataset to 13,304 events. The sky distribution of these events is shown in Fig. 7.

When performing a blind search for photon point sources, the probability p of obtaining a test statistic at least as extreme as the one that was actually observed is calculated, assuming an isotropic distribution. The test statistic is obtained from the ensemble of scrambled datasets (cf. Sec. 5), assuming a Poisson-distributed background. This p -value is calculated for a specific target direction as:

$$p = \text{Poiss}(\geq n_{\text{data}}^{\beta} | n_b^{\beta}) , \quad (6)$$

where $\text{Poiss}(\geq n_{\text{data}}^{\beta} | n_b^{\beta})$ is the Poisson probability to observe n_{data}^{β} or more events given a background expectation after β_{cut} of n_b^{β} . Note that the superscript “ β ” indicates the number of events after applying the optimized β_{cut} . The fraction of simulated datasets p_{chance} , in which the observed minimum p -value p_{min} is larger than or equal to the simulated p -value

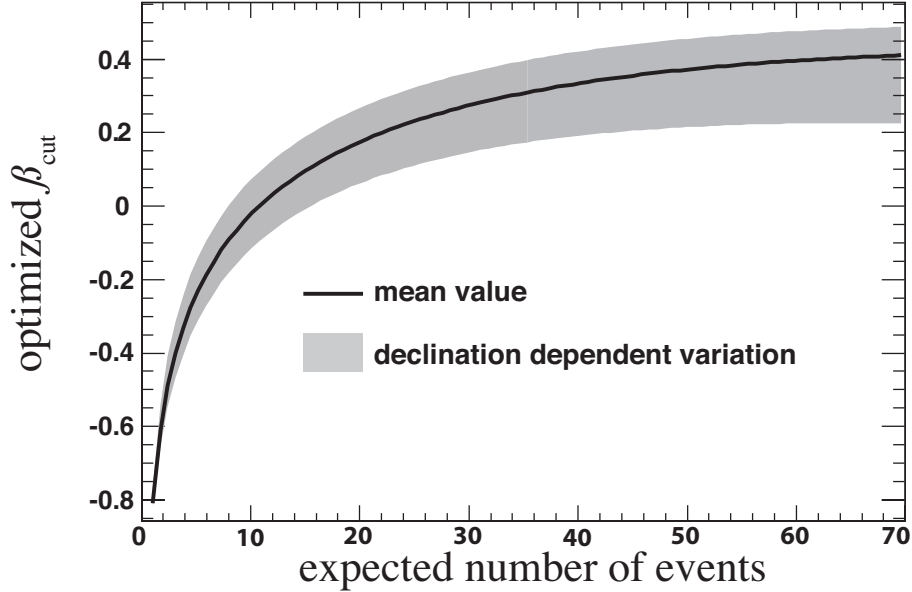


Fig. 6.— Optimized β_{cut} as a function of the expected background count. The mean value (solid black line) and the declination-dependent variations (shaded area) are illustrated.

$p_{\text{min}}^{\text{scr}}$, is given by:

$$p_{\text{chance}}(p_{\text{min}}^{\text{scr}} \leq p_{\text{min}}) . \quad (7)$$

This corresponds to the chance probability of observing p_{min} anywhere in the sky. The results when applying this blind search to the hybrid data of the Pierre Auger Observatory will be discussed in Sec. 8.

7. Upper limit calculation

Here we specify the method used to derive a skymap of upper limits to the photon flux of point sources. The directional upper limit on the photon flux from a point source is the limit on the number of photons from a given direction, divided by the directional acceptance (cf. Sec. 5) from the same target at a confidence level of $\text{CL} = 95\%$, and by a correction term:

$$f^{\text{UL}} = \frac{n_s^{\text{Zech}}}{n_{\text{inc}} \cdot \mathcal{E}_\beta} . \quad (8)$$

Here n_s^{Zech} is the upper limit on the number of photons obtained by using the β_{cut} definition in Fig. 6, and applying the procedure of Zech (cf. Eqn. (4)) for the observed number of events in data n_{data}^β :

$$P(\leq n_{\text{data}}^\beta | n_b^\beta + n_s^{\text{Zech}}) = \alpha_{\text{CL}} \cdot P(\leq n_{\text{data}}^\beta | n_b^\beta) . \quad (9)$$

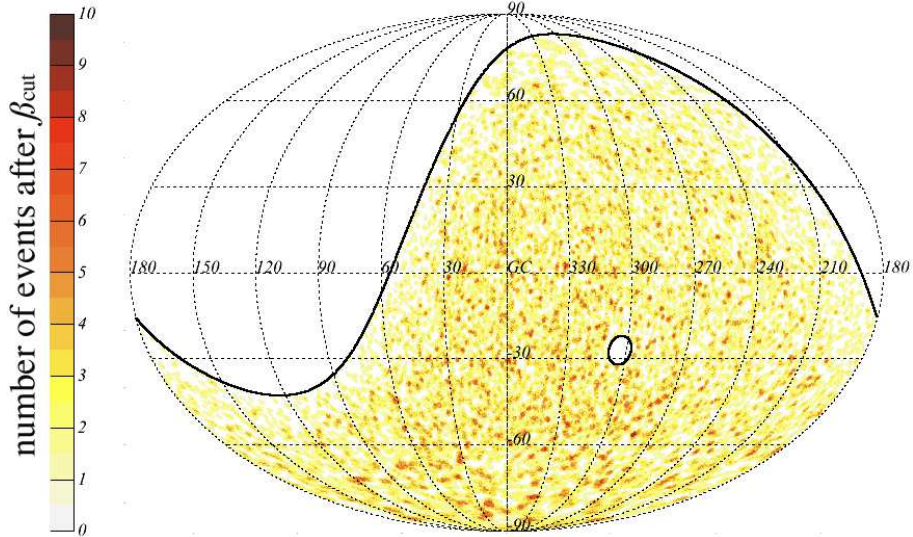


Fig. 7.— Sky map of measured events after applying the optimized β_{cut} illustrated in galactic coordinates.

The expected signal fraction in the top-hat search region is $n_{\text{inc}} = 0.9$, and \mathcal{E}_β is the total photon exposure. This latter exposure is derived as:

$$\mathcal{E}_\beta(\alpha, \delta) = \mathcal{E}(\alpha, \delta) \cdot \varepsilon_\gamma^\beta, \quad (10)$$

where \mathcal{E} indicates the exposure before applying the multivariate cut β_{cut} (cf. Eqn. 11), and ε_γ^β is the photon efficiency when applying a β_{cut} .

The exposure $\mathcal{E}(E)$ is typically defined as a function of energy E , cf. (The Pierre Auger Collaboration 2011a; Settimo 2012; The Pierre Auger Collaboration 2010d). In a similar way, the photon exposure \mathcal{E} as a function of celestial coordinates α and δ is defined as:

$$\mathcal{E}(\alpha, \delta) = \frac{1}{c_E} \int_E \int_T \int_S E^\zeta \varepsilon(E, t, \theta, \phi, x, y) \, dS \, dt \, dE, \quad (11)$$

where the coordinates α and δ are functions of the zenith (θ) and azimuth (ϕ) angles and of the time t ; ε is the overall efficiency including detection, reconstruction and selection of the events and the evolution of the detector in the time period T . The integration over energy is performed assuming a power-law spectrum with index $\zeta = -2$ and normalization factor $c_E = \int E^\zeta \, dE$. The area S encloses the full detector array and is chosen sufficiently large to ensure a negligible (less than 1%) trigger efficiency outside of it. The exposure for the hybrid detector is not constant with energy and is not uniform in right ascension. Thus, detailed simulations were performed to take into account the status of the detector and the dependence of its performance with energy and direction (both zenith and azimuth). For

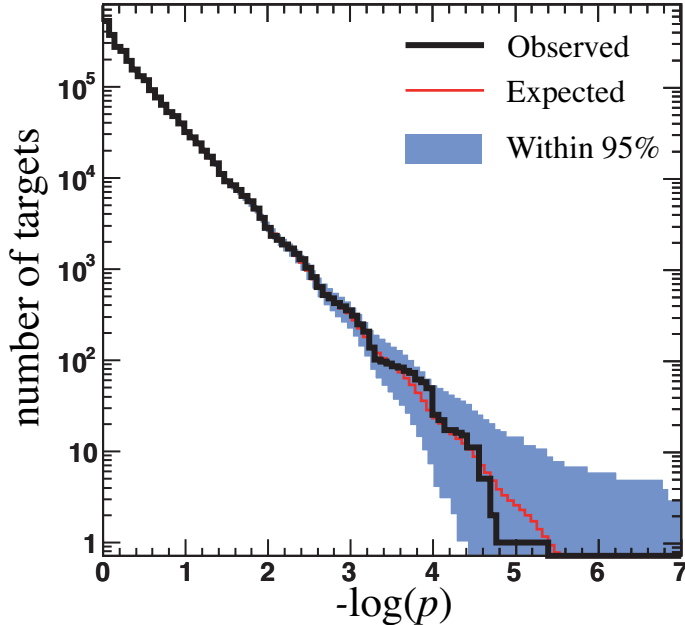


Fig. 8.— Integral distribution of p -values. For better visibility $-\log(p)$ is shown. The observed distribution is shown as a thick black line, the mean expected one, assuming background only, as a thin red line. The blue shaded region corresponds to 95% containment of simulated data sets.

the exposure calculation applied here, time-dependent simulations were performed, following the approach described in (The Pierre Auger Collaboration 2011a; Settimo 2012). This takes into account the photon trigger efficiency, possible periods of overcast cloud conditions, and offers the possibility of also investigating systematic uncertainties below the EeV range. At the low energy edge of $10^{17.3}$ eV, the hybrid trigger efficiency for photon-induced air showers is larger than 80%, rapidly increasing before reaching full efficiency at $10^{17.8}$ eV. Compared to hadron induced air showers, the photon trigger efficiency is always larger as a consequence of a later shower development, on average. The derived directional photon exposure has a mean of $180 \text{ km}^2 \text{ yr}$ and varies between $50 \text{ km}^2 \text{ yr}$ and $294 \text{ km}^2 \text{ yr}$. The impact of different photon spectral indices is discussed in Sec. 8. Directional upper limits on photons from point sources derived in this blind search analysis will be also discussed in Sec. 8.

8. Results and discussion

In the following, results on p -values and upper limits are given, based on the analysis method described in Sec. 6 and Sec. 7.

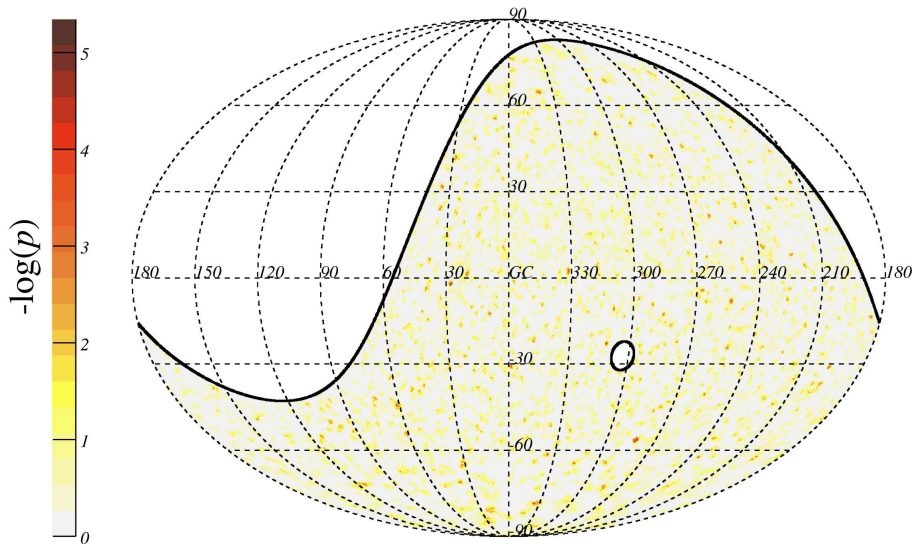


Fig. 9.— Celestial map of $-\log(p)$ values in Galactic coordinates.

The p -values, as defined in Eqn. 6, refer to a local probability that the data is in agreement with a uniform distribution. The integral distribution of $-\log(p)$ -values is shown in Fig. 8. The corresponding sky map of $-\log(p)$ -values is illustrated in Fig. 9. The minimum p -value observed is $p_{\min} = 4.5 \times 10^{-6}$ corresponding to a chance probability that p_{\min} is observed anywhere in the sky of $p_{\text{chance}} = 36\%$. This blind search for a flux of photons, using hybrid data of the Pierre Auger Observatory, therefore finds no candidate point on the pixelized sky that stands out among the large number of trials. It is possible that some genuine photon fluxes are responsible for some of the low p -values. If so, additional exposure should increase the significance of those excesses. They might also be identified in a future search targeting a limited number of astrophysical candidates. The present search, however, finds no statistical evidence for any photon flux.

Directional photon flux upper limits (95% confidence level) are derived using Eqn. (8) and shown as a celestial map in Fig. 10. The mean value is $0.035 \text{ photons km}^{-2} \text{ yr}^{-1}$, with a maximum of $0.14 \text{ photons km}^{-2} \text{ yr}^{-1}$. Those values correspond to an energy flux of $0.06 \text{ eV cm}^{-2} \text{ s}^{-1}$ and $0.25 \text{ eV cm}^{-2} \text{ s}^{-1}$, respectively, assuming an E^{-2} energy spectrum.

Various sources of systematic uncertainties were investigated and their impact on the mean flux upper limit is estimated. The systematics on the photon exposure ranges between $\pm 30\%$ at $10^{17.3} \text{ eV}$ and $\pm 10\%$ above 10^{18} eV and are dominated by the uncertainty on the Auger energy scale. A systematic uncertainty of the Auger energy scale of $+14\%$ and -14% (Verzi 2013) changes the mean upper limit by about $+8\%$ and -9% , respectively. Variations in determining the fraction of photon ($\epsilon_{\gamma}^{\beta}$) and measured events ($\epsilon_{\text{data}}^{\beta}$) passing a

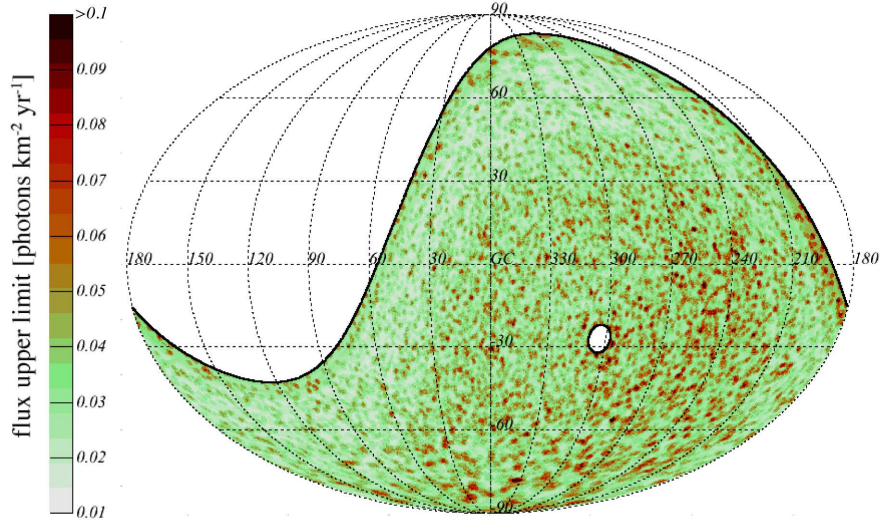


Fig. 10.— Celestial map of photon flux upper limits in photons $\text{km}^{-2} \text{yr}^{-1}$ illustrated in Galactic coordinates.

β_{cut} , introduced by, e.g., an additional directional dependency for photons, contribute less than 6%. A collection of $\sim 50,000$ proton CORSIKA air shower simulations, using EPOS LHC (Pierog *et al.* 2013), were additionally generated to estimate the impact of using a different high-energy hadronic interaction model. The resulting change of the mean limit of the photon flux is -9% . Furthermore, the assumed photon flux spectral index of -2 could be incorrect. To estimate the impact of this, the analysis is repeated assuming a spectral index of -1.5 or -2.5 . The mean upper limit changes by about -34% and $+51\%$, respectively, whereas the dominant contribution arises from a changing directional photon exposure, i.e., assuming a flatter primary photon spectrum increases the photon exposure, while reducing the average upper limits, and vice versa.

The limits are of considerable astrophysical interest in all parts of the exposed sky. The energy flux in TeV gamma rays exceeds $1 \text{ eV cm}^{-2} \text{ s}^{-1}$ for some Galactic sources with a differential spectral index of E^{-2} (Hinton & Hofmann 2009; H.E.S.S. Collaboration 2011). A source with a differential spectral index of E^{-2} puts out equal energy in each decade, resulting in an expected energy flux of $1 \text{ eV cm}^{-2} \text{ s}^{-1}$ in the EeV decade. No energy flux that strong in EeV photons is observed from any target direction, including directions of TeV sources such as Centaurus A or the Galactic center region. This flux would have been detected with $> 5\sigma$ significance, even after penalizing for the large number of trials (using Eqn. 6 and Eqn. 7). Furthermore, an energy flux of $0.25 \text{ eV cm}^{-2} \text{ s}^{-1}$ would yield an excess

of at least 5σ for median exposure targets. If we make the conservative assumption that all detected photons are at the upper energy bound, a flux of $1.44 \text{ eV cm}^{-2} \text{ s}^{-1}$ would be detectable. This result for median exposure targets is independent of the assumed photon spectral index, and implies that we can exclude a photon flux greater than $1.44 \text{ eV cm}^{-2} \text{ s}^{-1}$ with 5σ significance.

Results from the present study complement the blind search for fluxes of *neutrons* above 1 EeV previously published by the Auger Collaboration (The Pierre Auger Collaboration 2012b). No detectable flux was found in that search, and upper limits were derived for all directions south of declination $+20^\circ$. A future study will look for evidence of photon fluxes from particular candidate sources and “stacks” of candidates having astrophysical characteristics in common. A modest excess may be statistically significant if it is not penalized for a large number of trials. Neutrons and photons arise from the same types of pion-producing interactions. The photon path length exceeds the path length for EeV neutron decay, so this study is sensitive to sources in a larger volume than just the Galaxy.

The absence of detectable point sources of EeV neutral particles does not mean that the sources of EeV rays are extragalactic. It might be that EeV cosmic rays are produced by transient sources such as gamma ray bursts or supernovae. The Auger Observatory has been collecting data only since 2004. It is quite possible that it has not been exposed to neutral particles emanating from any burst of cosmic-ray production. Alternatively, it is conceivable that there are continuous sources in the Galaxy which emit in jets and are relatively few in number, and if so none of those jets are directed toward Earth. The protons would be almost isotropized by magnetic fields, but neutrons and gamma rays would retain the jet directions and would not arrive here. Another possibility is that the EeV protons originate in sources with much lower optical depth for escaping than is typical of the known TeV sources. The production of neutrons and photons at the source could be too meager to make a detectable flux at Earth.

The null results from this search for point sources of photons is nevertheless interesting in light of the stringent upper limits on cosmic-ray anisotropy at EeV energies (The Pierre Auger Collaboration 2012c,d, 2011b). EeV protons originating near the Galactic plane, whether from transient sources or steady sources, are expected to cause an anisotropy that exceeds the observational upper limit. Those expectations are not free of assumptions about magnetic field properties away from the Galactic disk, so the case against Galactic EeV proton sources is by no means closed. However, evidence for such sources remains absent, despite a sensitive search for any flux of EeV photons.

Acknowledgements

The successful installation, commissioning, and operation of the Pierre Auger Observatory would not have been possible without the strong commitment and effort from the technical and administrative staff in Malargüe.

We are very grateful to the following agencies and organizations for financial support: Comisión Nacional de Energía Atómica, Fundación Antorchas, Gobierno De La Provincia de Mendoza, Municipalidad de Malargüe, NDM Holdings and Valle Las Leñas, in gratitude for their continuing cooperation over land access, Argentina; the Australian Research Council; Conselho Nacional de Desenvolvimento Científico e Tecnológico (CNPq), Financiadora de Estudos e Projetos (FINEP), Fundação de Amparo à Pesquisa do Estado de Rio de Janeiro (FAPERJ), São Paulo Research Foundation (FAPESP) Grants # 2010/07359-6, # 1999/05404-3, Ministério de Ciência e Tecnologia (MCT), Brazil; MSMT-CR LG13007, 7AMB14AR005, CZ.1.05/2.1.00/03.0058 and the Czech Science Foundation grant 14-17501S, Czech Republic; Centre de Calcul IN2P3/CNRS, Centre National de la Recherche Scientifique (CNRS), Conseil Régional Ile-de-France, Département Physique Nucléaire et Corpusculaire (PNC-IN2P3/CNRS), Département Sciences de l'Univers (SDU-INSU/CNRS), France; Bundesministerium für Bildung und Forschung (BMBF), Deutsche Forschungsgemeinschaft (DFG), Finanzministerium Baden-Württemberg, Helmholtz-Gemeinschaft Deutscher Forschungszentren (HGF), Ministerium für Wissenschaft und Forschung, Nordrhein Westfalen, Ministerium für Wissenschaft, Forschung und Kunst, Baden-Württemberg, Germany; Istituto Nazionale di Fisica Nucleare (INFN), Ministero dell'Istruzione, dell'Università e della Ricerca (MIUR), Gran Sasso Center for Astroparticle Physics (CFA), CETEMPS Center of Excellence, Italy; Consejo Nacional de Ciencia y Tecnología (CONACYT), Mexico; Ministerie van Onderwijs, Cultuur en Wetenschap, Nederlandse Organisatie voor Wetenschappelijk Onderzoek (NWO), Stichting voor Fundamenteel Onderzoek der Materie (FOM), Netherlands; National Centre for Research and Development, Grant Nos. ERA-NET-ASPERA/01/11 and ERA-NET-ASPERA/02/11, National Science Centre, Grant Nos. 2013/08/M/ST9/00322 and 2013/08/M/ST9/00728, Poland; Portuguese national funds and FEDER funds within COMPETE - Programa Operacional Factores de Competitividade through Fundação para a Ciência e a Tecnologia, Portugal; Romanian Authority for Scientific Research ANCS, CNDI-UEFISCDI partnership projects nr.20/2012 and nr.194/2012, project nr.1/ASPERA2/2012 ERA-NET, PN-II-RU-PD-2011-3-0145-17, and PN-II-RU-PD-2011-3-0062, the Minister of National Education, Programme for research - Space Technology and Advanced Research - STAR, project number 83/2013, Romania; Slovenian Research Agency, Slovenia; Comunidad de Madrid, FEDER funds, Ministerio de Educación y Ciencia, Xunta de Galicia, Spain; The Leverhulme Foundation,

Science and Technology Facilities Council, United Kingdom; Department of Energy, Contract No. DE-AC02-07CH11359, DE-FR02-04ER41300, and DE-FG02-99ER41107, National Science Foundation, Grant No. 0450696, The Grainger Foundation, USA; NAFOSTED, Vietnam; Marie Curie-IRSES/EPLANET, European Particle Physics Latin American Network, European Union 7th Framework Program, Grant No. PIRSES-2009-GA-246806; and UNESCO.

REFERENCES

- Aharonian, F., & Neronov, A. 2005, *ApJ*, **619**, 306
- Alexandreas, D. E., Berley, D., Biller, S., Dion, G. M., Goodman, J. A., Haines, T. J., Hoffman, C. M., & Horch, E. *et al.* 1993, *NIMPA*, **328**, 570
- Argiro, S., *et al.* 2007, *NIMPA*, **580**, 1485
- Barbosa, H. M. J., Catalani, F., Chinellato, J. A., & Dobrigkeit, C. 2004, *APh*, **22**, 159
- BenZvi, S. Y. *et al.* 2007, *NIMPA*, **574**, 171
- Berezinsky, V., Gazizov, A. Z. & Grigorieva, S. I. 2006 *PhRvD*, **74**, 043005
- Bossa, M., Mollerach, S., & Roulet, E. 2003, *JPhG*, **29**, 1409
- Breiman, L., Friedman, J., Olshen, R., & Stone, C. 1984, Monterey (CA), Wadsworth and Brooks
- Bugayevskiy, L. M., & Snyder, J. P. 1995, Taylor & Francis London ; Bristol, PA
- Cassiday, G. L., *et al.* 1990, *NuPhS*, **14A**, 291
- Chirinos, J. (for the Pierre Auger Collaboration) 2013 Proc. 33rd ICRC, Rio de Janeiro, Brazil, 994
- Crocker, R. M., Fatuzzo, M., Jokipii, R., Melia, F., & Volkas, R. R. 2005, *ApJ*, **622**, 892
- De Angelis, A., Galanti, G., & Roncadelli, M. 2013 *MNRAS*, **432**, 3245
- Fermi-LAT Collaboration 2013, *Sci* **339**, 807
- Fesefeldt, H. 1985 Report **PITHA-85/02**, RWTH Aachen
- Gaisser, T. K., & Hillas, A.M. 1977, Proc. 15th ICRC, Plovdiv, Bulgaria, 358

- Greisen, K. 1956, Progress in Cosmic Ray Physics **3**, 17. Ed: Wilson, J.G., North-Holland, Amsterdam
- Greisen, K. 1966 PhRvL, **16**, 748
- Gorski, K. M., *et al.* 2005, ApJ, **622**, 759
- Gupta, N. 2012, APh, **35**, 503
- Heck, D., *et al.* 1998 Report FZKA, 6019
- H.E.S.S. Collaboration 2011, A&A, **528**, A143
- Hillas, A. M. 1984, ARA&A, **22**, 425
- Hinton, J. A., & Hofmann, W. 2009, ARA&A, **47**, 523
- Homola, P., & Risse, M. 2007, MPLA, **22**, 749
- Kalmykov, N. N., & Ostapchenko, S. S. 1989, SvJNP, **50**, 315 [YaFiz, **50**, 509]
- Kuempel, D. 2011, PhDT, Bergische Universität Wuppertal
- Medina Tanco, G. A., & Watson, A. A. 2001, Proc. 27th ICRC, Hamburg, Germany, 531
- Pierog, T., Karpenko, I., Katzy, J. M., Yatsenko, E., & Werner, K. 2013, DESY-13-125, arXiv:1306.0121
- Ros, G., Supanitsky, A. D., Medina-Tanco, G. A., del Peral, L., D'Olivo, J. C., & Rodriguez-Frias, M. D. 2011, APh, **35**, 140
- Ros, G., Supanitsky, A. D., Medina-Tanco, G. A., del Peral, L., & Rodriguez-Fras, M. D. 2013, APh, **47**, 10
- Schapire, R. E. 1990, Mach. Learn., **5**, 197
- Settimo, M. (for the Pierre Auger Collaboration) 2011, Proc. 32nd ICRC, Beijing, China, **2**, 55
- Settimo, M. (for the Pierre Auger Collaboration) 2012, EPJP, **127**, 87
- Settimo, M., & De Domenico, M. 2013 Proc. 33rd ICRC, Rio de Janeiro, Brazil, 918
- The Pierre Auger Collaboration 2004, NIMPA, **523**, 50
- The Pierre Auger Collaboration 2007, APh, **27**, 155

The Pierre Auger Collaboration 2008a, NIMPA, **586**, 409
The Pierre Auger Collaboration 2008b, APh, **29**, 243
The Pierre Auger Collaboration 2009, Aph, **31**, 399
The Pierre Auger Collaboration 2010a, PhRvL, **104**, 091101
The Pierre Auger Collaboration 2010b, NIMPA, **620**, 227
The Pierre Auger Collaboration 2010c, NIMPR, A613, 29
The Pierre Auger Collaboration 2010d, PhLB, **685**, 239
The Pierre Auger Collaboration 2011a, APh, **34**, 368
The Pierre Auger Collaboration 2011b, APh, **34**, 627
The Pierre Auger Collaboration 2012a, PhRvL, **109**, 062002
The Pierre Auger Collaboration 2012b, ApJ, **760**, 148
The Pierre Auger Collaboration 2012c, ApJS, **203**, 34
The Pierre Auger Collaboration 2012d, ApJ, **762**, L13
The Pierre Auger Collaboration 2013, JCAP, **02**, 026
Verzi, V. (for the Pierre Auger Collaboration) 2013, Proc. 33rd ICRC, Rio de Janeiro, Brazil, 928
Zatsepin, G. T. & Kuz'min, V. A. 1966, PZETF, 4(3), 114
Zech, G. 1989, NIMPA, **A277**, 608